International Journal of Nanomedicine

Dovepress
open access to scientific and medical research

Open Access Full Text Article

ORIGINAL RESEARCH

Gallium Metal–Organic Nanoparticles with Albumin-Stabilized and Loaded Graphene for Enhanced Delivery to HCT116 Cells

Yuan-yuan Wu[1], Wen-Hui Liao[1], Zong-ling Niu[1], Si-Han Zhou[1], Tian-Tian Wu[1], Zhe Li[2], Qi-Hua Zhao[1], Jing-Yuan Xu[2], Ming-jin Xie[1]

[1]School of Chemical Science and Technology, Yunnan University, Kunming, People's Republic of China; [2]Department of Chemical Biology and Tianjin Key Laboratory on Technologies Enabling Development of Clinical Therapeutics and Diagnostics (Theranostics), School of Pharmacy, Tianjin Medical University, Tianjin, People's Republic of China

Correspondence: Ming-jin Xie, Email mjxie@ynu.edu.cn

Background: Gallium (III) metal-organic complexes have been shown to have the ability to inhibit tumor growth, but the poor water solubility of many of the complexes precludes further application. The use of materials with high biocompatibility as drug delivery carriers for metal-organic complexes to enhance the bioavailability of the drug is a feasible approach.

Methods: Here, we modified the ligands of gallium 8-hydroxyquinolinate complex with good clinical anticancer activity by replacing the 8-hydroxyquinoline ligands with 5-bromo-8-hydroxyquinoline (HBrQ), and the resulting Ga(III) + HBrQ complex had poor water solubility. Two biocompatible materials, bovine serum albumin (BSA) and graphene oxide (GO), were used to synthesize the corresponding Ga(III) + HBrQ complex nanoparticles (NPs) BSA/Ga/HBrQ NPs and GO/Ga/HBrQ NPs in different ways to enhance the drug delivery of the metal complex.

Results: Both of BSA/Ga/HBrQ NPs and GO/Ga/HBrQ NPs can maintain stable existence in different solution states. In vitro cytotoxicity test showed that two nanomedicines had excellent anti-proliferation effect on HCT116 cells, which shown higher level of intracellular ROS and apoptosis ratio than that of cisplatin and oxaliplatin. In addition, the superior emissive properties of BSA/Ga/HBrQ NPs and GO/Ga/HBrQ NPs allow their use for in vivo imaging showing highly effective therapy in HCT116 tumor-bearing mouse models.

Conclusion: The use of biocompatible materials for the preparation of NPs against poorly biocompatible metal-organic complexes to construct drug delivery systems is a promising strategy that can further improve drug delivery and therapeutic efficacy.

Keywords: gallium complex, nanomedicine, anticancer, colorectal cells, drug delivery, in vivo imaging

Introduction

Early studies demonstrated that gallium nitrate[1] or gallium chloride have been developed as antitumor drug candidates.[2–4] On account of high nephrotoxicity and complicated in vivo speciation, gallium nitrate was limited in clinical trials.[5,6] The limitations with gallium nitrate and gallium chloride make the development of strategies that could adequately exploit the affinity of gallium for tumor tissues and avoid severe toxic effects. A series of oral gallium complexes such as gallium maltolate (GaM)[7–9] or tris(8-quinolinolato)gallium(III) (KP46)[7,10–12] have been developed to circumvent these drawbacks, which show promise to initiate a revival of gallium in the clinical setting. Encouraged by the results of GaM and KP46 in clinical trials, novel Ga(III) complexes with preclinical antitumor activity exploited.[13–15] Researchers are very interested in exploring more gallium(III) complexes with other reasonable substituents of 8-hydroxyquinoline ligands, among which 5-bromo-8-hydroxyquinoline (HBrQ) has been shown to have some anticancer activity in the study,[16,17] so HBrQ can be selected as an organic ligand for gallium(III) complex. On the other hand, due to pharmacological inadequacies such limited bioavailability,[18] poor water solubility,[19] drug resistance, and short circulation durations, the fast development of metal-complexed medications poses additional difficulties.[20] A promising strategy have been

Received: 25 August 2022
Accepted: 12 December 2022
Published: 13 January 2023

Graphical Abstract

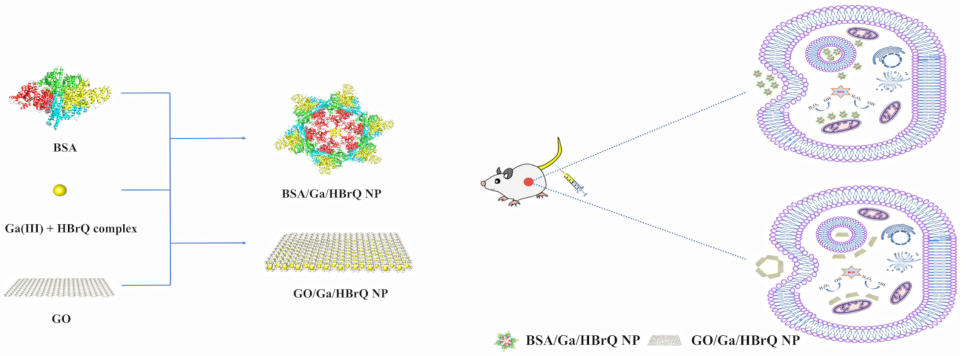

explored appropriate drug delivery system to enhance the solubility of metal-based anticancer agents,[21–23] prolong their half-life in vivo,[24–26] inhibit the development of drug resistance,[27–30] and enable their controlled release into tumor tissues.[31–34]

Bovine serum albumin (BSA) has the property of strong affinity for binding various organic molecules at different sites, which enables the utilization of BSA-modified nanoparticles (NPs) in various supramolecular assemblies. In addition to BSA, graphene oxide (GO) has a large surface area and is also excellent in hydrophilicity and biocompatibility.[35] Most importantly, functional materials of BSA and GO have been widely used as platforms for loading NPs, both of which are widely used as multifunctional drug delivery vehicles.[36–40] In addition, tumor cells will rapidly ingest nano drugs by endocytosis, and then release the synthesized metal complex drugs, which not only improves the inhibitory effect of metal complex drugs on tumors, but also solves the problem of systemic drug delivery of metal complex drugs.[41–43]

In this study, metal-organic nanomedicines BSA/Ga/HBrQ NPs and GO/Ga/HBrQ NPs, consisting of BSA or GO complexed with Ga(III)+HBrQ, were developed using BSA and GO as drug delivery carriers, respectively. These two nanomedicines showed better biocompatibility and solubility in physiological solutions. The inhibitory effects of BSA/Ga/HBrQ NPs and GO/Ga/HBrQ NPs on cancer cells were evaluated by in vitro cytotoxicity assays, and then the mechanisms by which BSA/Ga/HBrQ NPs and GO/Ga/HBrQ NPs inhibit tumor cells were explored by cell cycle, apoptosis, reactive oxygen species levels and mitochondrial membrane potential. Finally, the imaging and tumor targeting effects of both NPs in vivo were investigated. Ga(III) + HBrQ complex with BSA or GO as the delivery vehicle effectively enhanced the bioavailability of Ga(III) + HBrQ complex and showed efficient therapeutic effects in HCT116 cells. These results provide new developmental ideas for the rational design of nanoparticles and convenient preparation for drug delivery of metal complexes with poor biocompatibility.

Experimental Procedures

Materials and Methods

All reagents and solvents used in the experiments were commercially available and used without further purification. PBS buffer (1X, pH 7.2–7.4, Adamas life, China). DCFH-DA (2',7'-Dichlorofluorescein diacetate, Beyotime Biotechnology, China). MTT (3-(4,5-dimethylthiazol-2-yl)-2,5-diphenyltetrazoli-um bromide), Annexin-V-FITC and propidium iodide (PI) (Solarbio, Beijing, China). Mitochondrial membrane potential assay kit with JC-1 (Beyotime Biotechnology, Shanghai, China). Gallium(III) nitrate nonahydrate ($Ga(NO_3)_3{\cdot}9H_2O$, Adamas, Shanghai, China). 5-Bromo-8-hydroxyquinoline (Adamas, Shanghai, China). Cisplatin (Macklin, Shanghai, China). Oxaliplatin (Leyan, Shanghai, China). Ultrapure water (18 M Ω·cm resistivity from an EASY Ultra-pure Water System, Heal Force, Shanghai, China) was used in the experiments. MCE membrane filters (0.22 μm, Jinteng, Tianjin, China) for suction filtration were used. The microwave synthesizer (SP, UWave-2000, SINEO, Shanghai, China) for the reaction was used.

Synthesis of BSA/Ga/HBrQ NPs

The BSA/Ga/HBrQ NPs was prepared by referring to a previously reported protein-nanoreactor method.[41,44] BSA (100 mg) was dissolved in 20 mL of ultrapure water in a round bottom flask. And under magnetic stirring, added 100 μL NaOH (1M) was to the protein solution until it was completely dissolved. After that, 500 μL of $Ga(NO_3)_3$ (100 mM) and 2.2 mL of HBrQ acetone solution (75 mM) were added to the above solution at the same time. Then, the mixture changed from colorless to pale yellow. The mixture was stirred at room temperature for 48 hours to remove the solvent acetone. The obtained BSA/Ga/HBrQ NPs was purified by dialysis for 48 hours (MW 10kDa). After lyophilization, the sample is in 167.8 mg (79.59%) and stored at 4°C for later use.

Synthesis of GO/Ga/HBrQ NPs

The GO/Ga/HBrQ was prepared by referring to the previously reported protein-nanoreactor method.[45] The GO was dissolved in 25 mL of water to form a 4 mg/mL GO dispersion. After that, 500 μL of $Ga(NO_3)_3$ (100 mM) and 500 μL of HBrQ acetone solution (300 mM) were added to the above solution at the same time. Put the solution in a microwave synthesizer (SP, UWave-2000, SINEO, Shanghai, China), heat to 105°C under high-speed stirring, hold for 2.5 minutes, and then quickly cool to 60°C with compressed air and flowed naturally. Cool to room temperature. The GO/Ga/HBrQ NPs reaction solution was purified by suction filtration with a 0.1 μm Millipore filter, and the filter cake was resuspended in ultrapure water for 10 min. Repeated the above purification step at least 3 times to fully remove unreacted reagents. After lyophilization, the sample was 157.4 mg (74.65%) and stored at 4°C for later use.

Characterization

Inductively coupled plasma mass spectrometry (ICP-MS) was recorded on a 7700x (Agilent, USA) spectrometer. The ultraviolet-visible (UV-vis) spectra were performed on a Hitachi U-4100 spectrometer. The Fourier transform infrared (FTIR) spectra were acquired by a Thermo Scientific FTIR-Nicolet iS10 spectrometer in the range 4000−400 cm^{-1}. Dynamic light scattering (DLS) and zeta potential were performed at 25°C on Zetasizer Nano ZS90 (Malvern Instruments Ltd, UK). The morphology and energy-dispersive spectroscopy (EDS) data of BSA/Ga/HBrQ NPs and GO/Ga/HBrQ NPs were obtained using a Nova NanoSEM 450 field-emission scanning electron microscope (SEM) at 10 kV and using a JEM-2100 transmission electron microscope (TEM) at 200 kV, and X-ray spectroscopy (XPS) data were acquired using a K-Alpha+ X-ray photoelectron spectrum. Luminescence spectroscopy analysis of BSA/Ga/HBrQ NPs and GO/Ga/HBrQ NPs was performed on a Lengguang (Shanghai, China) F98 fluorescence spectrophotometer. Cells were counted by Countstar cell automatic counter from Advanced Lab Instrument & Technology Co., Ltd. Microplate Reader (Infinite® 200 Pro NanoQuan, Tecan, Swiss). Flow Cytometry was performed on a BD FACS Canto II flow cytometer. Small Animal Live Imaging System (PerkinElmer IVIS, USA).

Loading Determination of Nanomedicines

The absorbance of the PBS solution of HBrQ at 320 nm was measured, and the standard curve of the concentration absorbance of HBrQ was drawn. The BSA/Ga/HBrQ NPs and GO/Ga/HBrQ NPs solution were prepared with PBS, and the absorbance of HBrQ was measured under the same conditions. For the quantitative analysis of Ga in BSA NP and GO NP solutions. 100 mL of 1 mg/mL of BSA NP and GO NP solutions were prepared with an aqueous solution containing nitric acid (v/v ≦ 2%), respectively, and completely digested at room temperature for 24 h. Then, 10 mL of samples were taken and analyzed by ICP-MS.

The amount of loaded anticancer agent was calculated according to the standard curve, and the yield and drug loading (DLC) were calculated according to the formula:[41]

$$\text{Yield} = \left(m_{\text{original HBrQ}} - m_{\text{measured}}\right) / m_{\text{theoretical anticancer agent}}$$

$$\text{Drug loading} = m_{\text{loaded anticancer agent}} / m_{\text{nano-drug}}$$

Cell Culture

Human epithelial cervical cancer HeLa cells, human colon cancer HCT116 cells, human breast cancer MDA-MB-231 cells and human normal liver cells LO2 were obtained from the American Type Culture Collection (ATCC). The cells were maintained in either DMEM medium (for HeLa, MDA-MB-231 and LO2), or RPMI 1640 medium (for HCT116) containing 10% FBS at a humidified atmosphere containing 5% CO_2 at 37°C.

Cytotoxicity Assays

The cytotoxicity assays of complexes were assessed by the MTT staining method. First, the different cells were seeded in 96-well plates at a density of 3×10^3 cells per well and grown in the medium for 24 h. After attachment, the cells were exposed to tested complexes at the graded concentration for 48 h. At the end of the incubation period, 10 μL MTT solution in PBS (5 mg/mL) was added and incubated at 37 °C for another 4 h. Then the supernatant was removed and 100 μL DMSO was added to dissolve the formazan crystals. The absorbance values at 570 nm were detected on Microplate Reader. Each experiment was executed in triplicate.

Cell Cycle Distribution

For the cell cycle assay, HCT116 cells were seeded in 6-well plates, and cultured for 24 hours. Then discarded the previous culture medium and use fresh medium cultured including NPs and complexes (10 μM) and PBS as a control for another 24 hours. After treatment, cells were fixed. They were then washed with cold PBS, 1 μL of propidium iodide (PI) was added, and stained in the dark for 30 min. The assay was subsequently performed on a flow cytometer and the cell cycle was analyzed with FlowJo software to determine cell cycle distribution. These assays were repeated three times.

Cell Apoptosis Assay

For the cell apoptosis assay, HCT116 cells were seeded in 6-well plates cultured for 24 hours. Then discarded the previous culture medium and use fresh medium cultured including NPs and complexes (10 μM) and PBS as a control for another 24 hours. After treatment, cells were fixed. Then, 5 μL Annexin-V/PI staining solution was added and stained in the dark for 30 min. Apoptosis was detected by flow cytometry, and statistical analysis of the results was done with the aid of FlowJo software, and these assays were repeated three times.

Reactive Oxygen Species (ROS) Detection

In this study, DCFH-DA was converted to 2',7'-dichlorofluorescein (DCFH), which was used as a probe for ROS generation. The level of ROS in HCT116 cells was measured using a ROS species assay kit. HCT116 cells were seeded in a 6-well plate at a density of 1×10^6 cells/well, cultured at 37°C, 5% CO_2 for 24 h, and then selected drugs (10 μM) and PBS, and continued After 48 hours of culture, cells were fixed. An appropriate volume of diluted DCFH-DA was added and incubated in a 37°C incubator for 20 min. The cells were then washed with PBS to remove the dye, and the fluorescence intensity of the cells was monitored by flow cytometry and confocal laser scanning microscopy, respectively. These measurements were repeated three times.

Mitochondrial Membrane Potential Assay

To observe the changes in mitochondrial membrane potential HCT116 cells, fluorescent inverted microscopy was used to observe the changes in intracellular mitochondrial membrane potential according to the guidelines of the JC-1 assay kit (Beyotime Biotechnology, Shanghai).

Animal and Tumor Models

All animals (BALB/c-nu, male, 4–6 weeks old) were purchased from SPF (Beijing) Biotechnology Co., Ltd. All animal procedures were approved by the Animal Experimentation Ethics Committee of Research selection Biotechnology (Hangzhou) Co., Ltd (permission number SYXK (Zhe Jiang) 2020–0043), and all procedures were performed in strict accordance with the Guide for the Care and Use of Laboratory Animals and the Regulation of Animal Protection Committee to minimize suffering and injury.

Establishment of orthotopic tumor model: Tumor model NU/NU nude mice 2 (male, 6 weeks) mice can freely drink water and standard chow at room temperature. An animal model of subcutaneous injection of HCT116 cells was established. Each nude mouse was subcutaneously injected with 2×10^6 HCT116 cell suspension and 100 μL of normal saline. Approximately 7 days after injection, tumor volume was grown to ~80 mm^3 and selected for in vivo experiments. The formula for calculating the tumor volume in mice is:

$TumorVolume(V) = width^2 \times length \times 0.5$, Relative tumor volumes were calculated as V/V_0.

In vivo Imaging and Biodistribution Study

HCT116 cells bearing nude male mice were intravenously injected via tail vein with 200 μL BSA/Ga/HBrQ NPs or GO/Ga/HBrQ NPs (10 μM). Fluorescence intensity was monitored using an in vivo imaging system (PerkinElmer IVIS) with a set wavelength. (λex = 420 nm, λem = 540 nm).

Statistical Analysis

The data were shown as mean ± standard deviation (SD) and the significance between two groups of the data in this work was analyzed based on student's two-tailed *t*-test (*p < 0.05, **p < 0.01, ***p < 0.001, ****p < 0.0001).

Results and Discussion

Preparation and Characterization of BSA/Ga/HBrQ NPs and GO/Ga/HBrQ NPs

As shown in Scheme 1, BSA/Ga/HBrQ NPs and GO/Ga/HBrQ NPs were synthesized using either BSA or GO as nanoreactors. Based on BSA showing its tertiary configuration, abundant active groups such as mercaptans and carboxyl groups are exposed in amino acid residues. GO can be used as a good carrier for carrying and stabilizing various nanomaterials due to its good planarity and super high surface-to-volume ratio. The complex formed by $Ga(NO_3)_3$ and HBrQ was wrapped by unfolded BSA or GO and stabilized by the active groups in the protein and GO.

The size and morphology of the BSA/Ga/HBrQ NPs and GO/Ga/HBrQ NPs were confirmed with the help of DLS and transmission electron microscopy (TEM). As shown in Figure 1A, the hydrodynamic diameter of BSA/Ga/HBrQ NPs nanomedicine is about 110.5 nm, which helps to enhance its accumulation in tumor tissues by EPR effect and avoid rapid excretion by the kidney.[46] Meanwhile, TEM images showed that BSA/Ga/HBrQ NPs was spherical with an average size of about 100 nm, which was slightly smaller than the results of DLS. This is due to the shrinkage of the protein during the TEM sample preparation. As shown in Figure 1B, the GO/Ga/HBrQ nanocomposites are presented as a monolayer with a GO base. The observed black dots are Ga/HBrQ NPs, which are spherical in shape and are uniformly attached to the entire surface of the nanocomposite with high density.[46] And since GO as a two-dimensional material has a large hydrodynamic diameter, the particle size range of GO/Ga/HBrQ composites is about 500 nm-900 nm, with an average particle size of 669.0 nm, and the particle size of Ga/HBrQ NPs measured on GO/Ga/HBrQ is about 59 nm (Figure S1). These results suggest that BSA is wrapping Ga(III) + HBrQ complex to form NPs, while GO is acting as the basic skeleton of GO/Ga/HBrQ, providing the anchor for Ga/HBrQ NPs BSA wraps Ga(III) + HBrQ complex to form NPs to fixate while preventing aggregation.

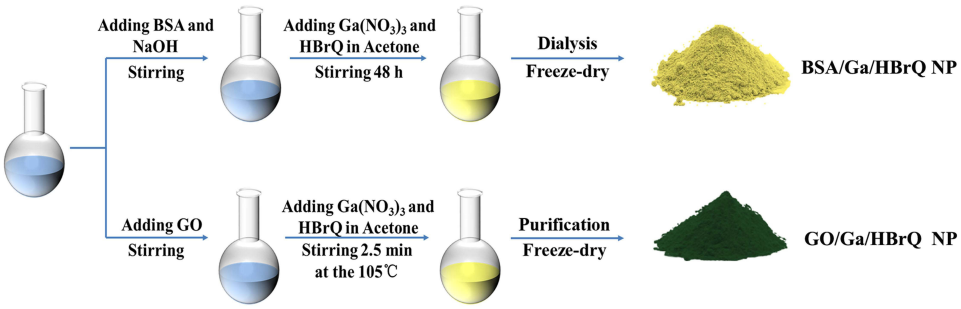

Scheme 1 The schematic diagram for the construction procedure of BSA/Ga/HBrQ NPs and GO/Ga/HBrQ NPs.

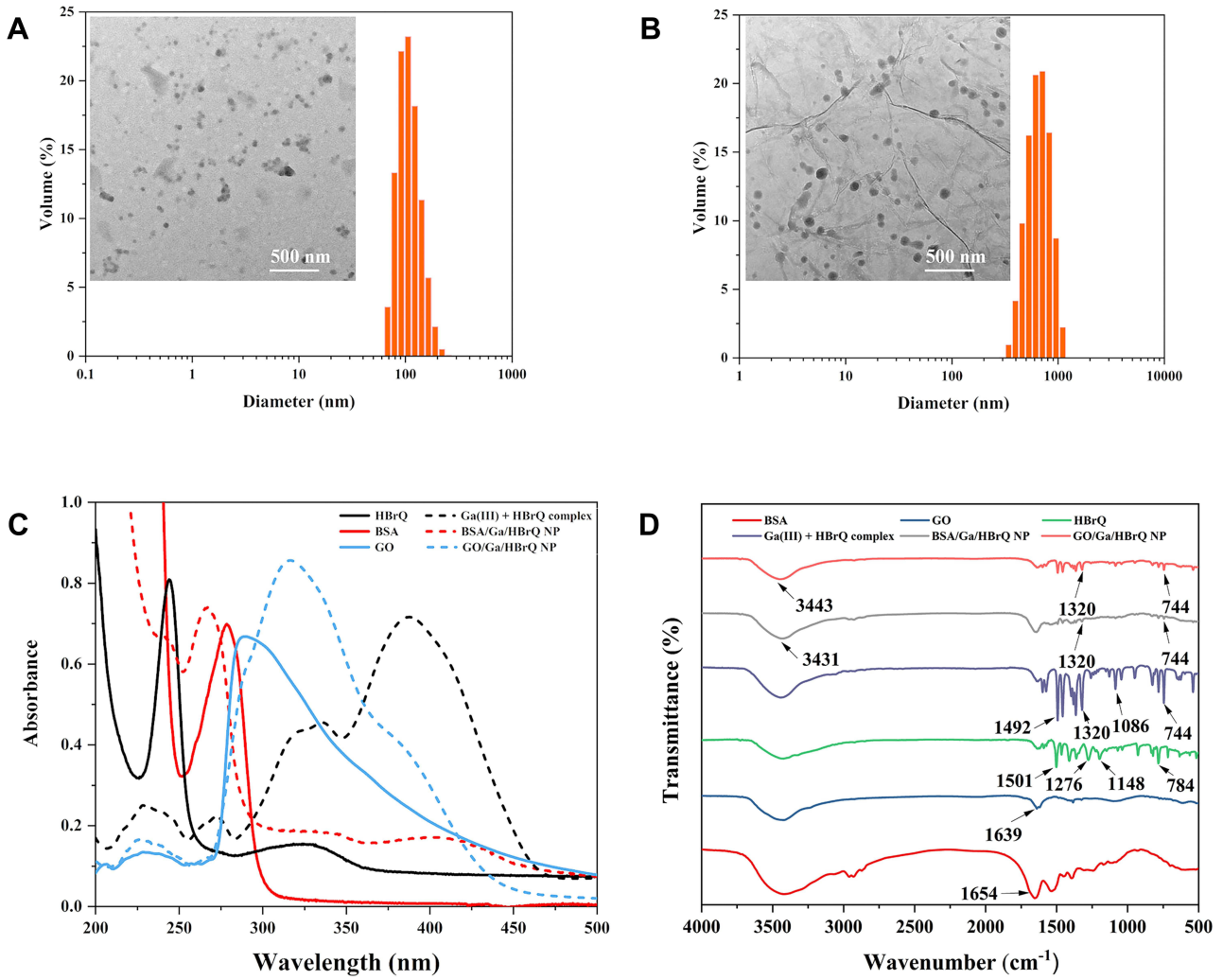

Figure 1 DLS data of (**A**) BSA/Ga/HBrQ NPs and (**B**) GO/Ga/HBrQ NPs. The inset shows their corresponding TEM images (**C**) UV-vis absorbance spectra of BSA, GO, HBrQ, Ga(III) + HBrQ complex, BSA/Ga/HBrQ NPs and GO/Ga/HBrQ NPs. (**D**) FT-IR spectra of BSA, GO, HBrQ, Ga(III) + HBrQ complex, BSA/Ga/HBrQ NPs and GO/Ga/HBrQ NPs.

The Zeta potential after drug loading on the carrier to form NPs was different from that before loading: −17.83 ± 1.36 mV for BSA and −34.5 ± 0.92 mV for GO before loading, and −10.33 ± 0.85 mV and −33.7 ± 0.89 mV for both NPs after loading with Ga(III) + HBrQ complexes with positive Zeta potential. From a biopharmaceutical point of view, a negative Zeta potential is an advantage because the nanoparticles with a negative surface charge reduce the bio-adhesion of plasma proteins and have a low non-specific cellular uptake rate, thus facilitating the uptake of nanomedicines by cancer cells[47] (Figure S2).

To verify whether the Ga(III) + HBrQ complex is contained in the nanomedicine, the UV-visible light absorption spectra of HBrQ, BSA, $Ga(NO_3)_3$, Ga(III) + HBrQ complex and two nanomedicines were measured separately. As shown in Figure 1C, pure HBrQ has two distinct characteristic absorption peaks, which are 244 nm and 323 nm, respectively. After adding $Ga(NO_3)_3$, the Ga(III) + HBrQ complex showed a broad absorption peak at 387 nm, which is a typical metal-to-ligand charge transfer (MLCT) characteristic.[48,49] The BSA/Ga/HBrQ NPs also has a broad absorption peak near 387 nm, which is consistent with the characteristic MLCT absorption peak in the Ga(III) + HBrQ complex, which demonstrates the presence of Ga(III) + HBrQ complex in both NPs. The composition of BSA/Ga/HBrQ NPs and GO/Ga/HBrQ NPs was also characterized by FTIR (Figure 1D). The peaks at 1230, 744 cm^{-1} are indicated that there is a complex of gallium. In addition, pure HBrQ has two obvious absorption peaks of C-N and CO at 1276, and 1148 cm^{-1},

respectively. In addition, it can be seen from the spectra of BSA/Ga/HBrQ NPs, GO/Ga/HBrQ NPs, GO and BSA. Compared with GO and BSA, their -OH peak at ~3435 cm^{-1} is significantly weakened. During the process of Ga/HBrQ NPs binding, -OH may be electrostatically attracted. All these peaks appear in the spectrum of two nanomedicines indicating the presence of BSA or GO and HBrQ in BSA/Ga/HBrQ NPs and GO/Ga/HBrQ NPs.

The yields of the produced BSA/Ga/HBrQ NPs and GO/Ga/HBrQ NPs were calculated to be 79.59 and 74.65%, respectively, based on the equations for the loading determination of nanomedicines in Loading Determination of Nanomedicines. Combined with the determination of Ga content according to inductively coupled plasma mass spectrometry (ICP-MS) (Figure S3), the drug loading capacity (DLC) of BSA/Ga/HBrQ NPs and GO/Ga/HBrQ NPs was calculated to be 45.27 and 48.18%, respectively, which shows that GO and BSA are stronger than BSA in terms of drug loading effect for Ga(III) + HBrQ complex.

XPS, SEM, and EDXS were used to characterize the chemical forms and main element distribution of metal ions in BSA/Ga/HBrQ NPs and GO/Ga/HBrQ NPs. The XPS measurement showed that the main elements C, N, O, Br and Ga were presented on the surface of the two nano-drugs, while the BSA/Ga/HBrQ NPs also has element S due to the presence of protein (Figure 2A and B). The high-resolution XPS showed peaks at 1143.5 and 1116.5 eV that were assigned to Ga $2p_{1/2}$ and Ga $2p_{3/2}$, respectively (Figure 2A and B), which were consistent with the literature.[50,51] In addition, the peaks of 1143.5 and 1116.5 eV were related to the Ga ($3d^{10}$) species, confirming that the higher oxidation state of gallium as Ga^{3+}. The SEM images showed the 2D morphology of BSA/Ga/HBrQ NPs and GO/Ga/HBrQ NPs after freeze-drying (Figure 2C and D). The EDXS spectrum in Figure 2E revealed 61.32, 16.07, 20.65, 1.24, 0.50, and 0.22% of C, N, O, Br, S, and Ga in the surface of BSA/Ga/HBrQ NPs and Figure 2F revealed 66.64, 8.37, 19.29, 4.22, and 1.48% of C, N, O, Br, and Ga in the surface of GO/Ga/HBrQ NPs, respectively. The EDXS elemental mappings in Figure S4 of BSA/Ga/HBrQ NPs and Figure S5 of GO/Ga/HBrQ NPs. The aforementioned results confirmed that Ga/HBrQ NPs wrapped and immobilized by BSA and GO were successfully prepared.

Stability of BSA/Ga/HBrQ NPs and GO/Ga/HBrQ NPs in Various Media

Both BSA and GO are drug transport carriers with good biocompatibility. The instability of nanomaterials prepared on the basis of BSA or GO assemblies in physiological solutions not only diminishes their biological activity, but also seriously affects the durability of their potency. To evaluate the stability performance of both NPs in different solutions, stability analysis was performed on various nanomaterials dispersed in various solutions after resting treatment. It can be seen from Figure 3A that the color of the solution did not change significantly within seven days after BSA/Ga/HBrQ NPs and GO/Ga/HBrQ NPs were dissolved in ultrapure water, PBS buffer with pH=7.2–7.4, DMSO and DMF solutions, respectively; On this basis, the dynamic light scattering instrument (DLS) was used to measure the particle size change of the two nano prodrugs dissolved in ultra-pure water. As shown in Figure 3B and D, the particle size of BSA/Ga/HBrQ NPs and GO/Ga/HBrQ NPs changed slightly with time, but in general, there was no obvious phenomenon of sedimentation and agglomeration. In addition to testing stability at physiological pH (pH 7.4), the stability of both NPs was evaluated in vitro in PBS solutions with two different pH values (extra-tumor cell: pH ~6.8, endosomal: pH ~5 to 6).[52] As shown in Figure S6A, the particle size of BSA/Ga/HBrQ NP gradually increases with decreasing pH in PBS solution because BSA can lead to conformational isomerization and intermolecular aggregation due to pH change under non-physiological conditions;[53,54] meanwhile, the particle size of GO/Ga/HBrQ NP also increases with decreasing pH and cannot be stably dispersed in physiological solution, which is mainly due to the presence of various electrolytes in acidic solution, which can shield the surface charge of GO,[55] thus causing the loss of electrostatic repulsion between GO layers and stacking until aggregation occurs (Figure S6B). However, due to the poor solubility of Ga (III)+HBrQ complex (Figure S7), the use of BSA or GO can further optimize the biocompatibility. The above experiments can prove that BSA/Ga/HBrQ NPs and GO/Ga/HBrQ NPs have good stability in different solutions, and further prove that BSA and GO can be used to improve the biocompatibility of metal organic complexes.

The Cytotoxicity of BSA/Ga/HBrQ NPs and GO/Ga/HBrQ NPs to Cancer Cells

The cytotoxicity of BSA/Ga/HBrQ NPs, GO/Ga/HBrQ NPs and cisplatin as control was assessed by the standard MTT assay using HeLa, HCT-116, MDA-MB-231 three cancer cell lines and a normal cell lines LO2 and the results are

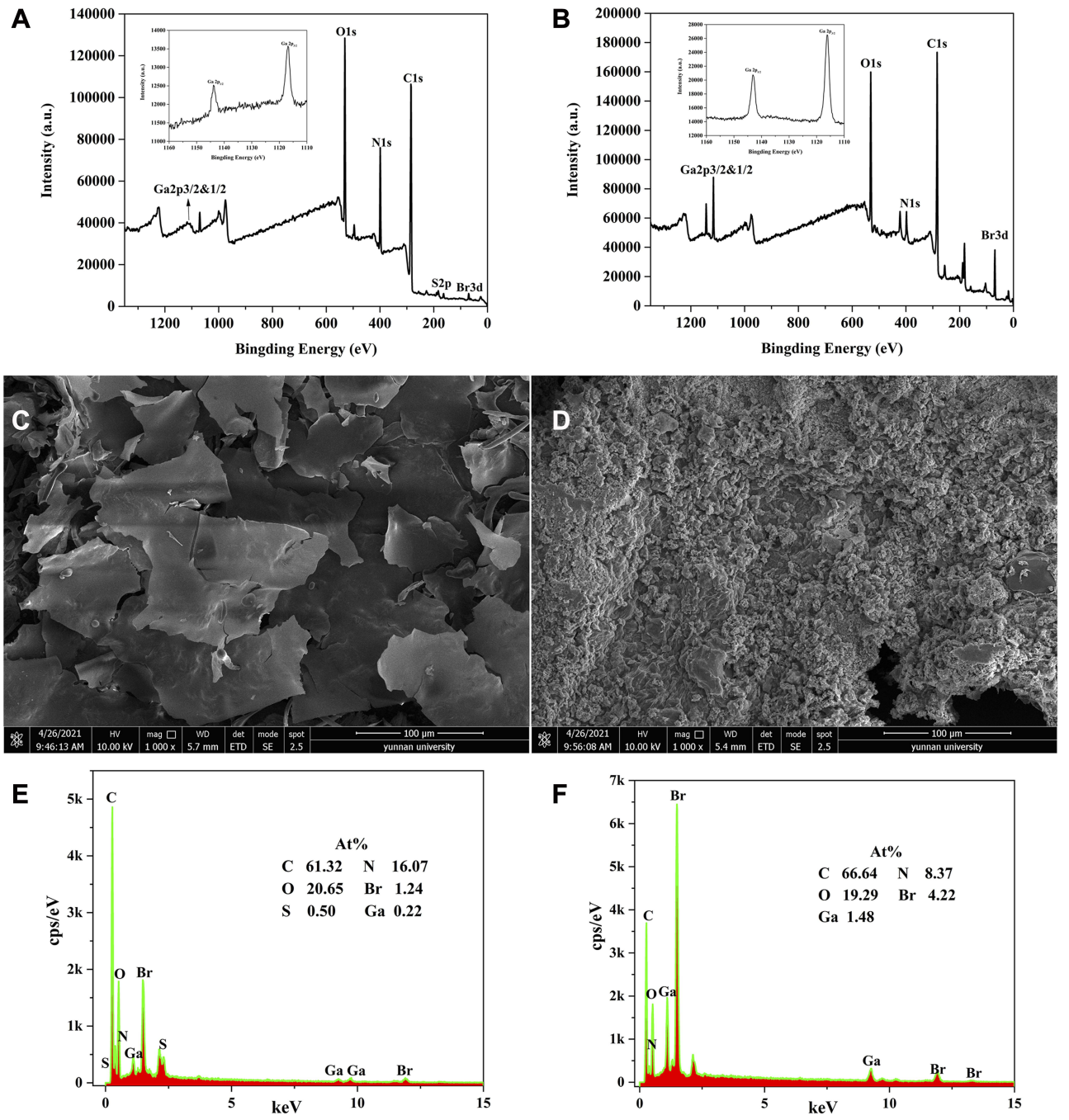

Figure 2 XPS spectrum of (**A**) BSA/Ga/HBrQ NPs, inset is XPS spectrum of Ga in the prepared BSA/Ga/HBrQ NPs and (**B**) GO/Ga/HBrQ NPs, inset is XPS spectrum of Ga in the prepared GO/Ga/HBrQ NPs; SEM image of (**C**) BSA/Ga/HBrQ NPs and (**D**) GO/Ga/HBrQ NPs; EDXS spectrum of (**E**) BSA/Ga/HBrQ NPs and (**F**) GO/Ga/HBrQ NPs.

summarized in Table 1. The growth of HCT-116 and MDA-MB-231 malignant tumor cells was strongly inhibited by BSA/Ga/HBrQ NPs and GO/Ga/HBrQ NPs within 48 hours. According to the IC_{50} values (Table 1), BSA/Ga/HBrQ NPs and GO/Ga/HBrQ NPs exhibited significant cytotoxicity against HCT-116 cells tested, the IC_{50} of BSA/Ga/HBrQ NPs (1.89 µM) and GO/Ga/HBrQ NPs (4.75 µM) was lower than that of cisplatin (9.08 µM). Besides, BSA/Ga/HBrQ NPs (9.37µM) and GO/Ga/HBrQ NPs (1.57 µM) also showed potentially good inhibition activity to MDA-MB-231 cells (IC_{50} of cisplatin is 12.21 µM). Importantly, BSA/Ga/HBrQ NPs (5.85µM) and GO/Ga/HBrQ NPs (8.29 µM) showed less toxicity than cisplatin (3.99 µM) in LO2 cells, which might reduce system toxicity of cisplatin. In addition, we

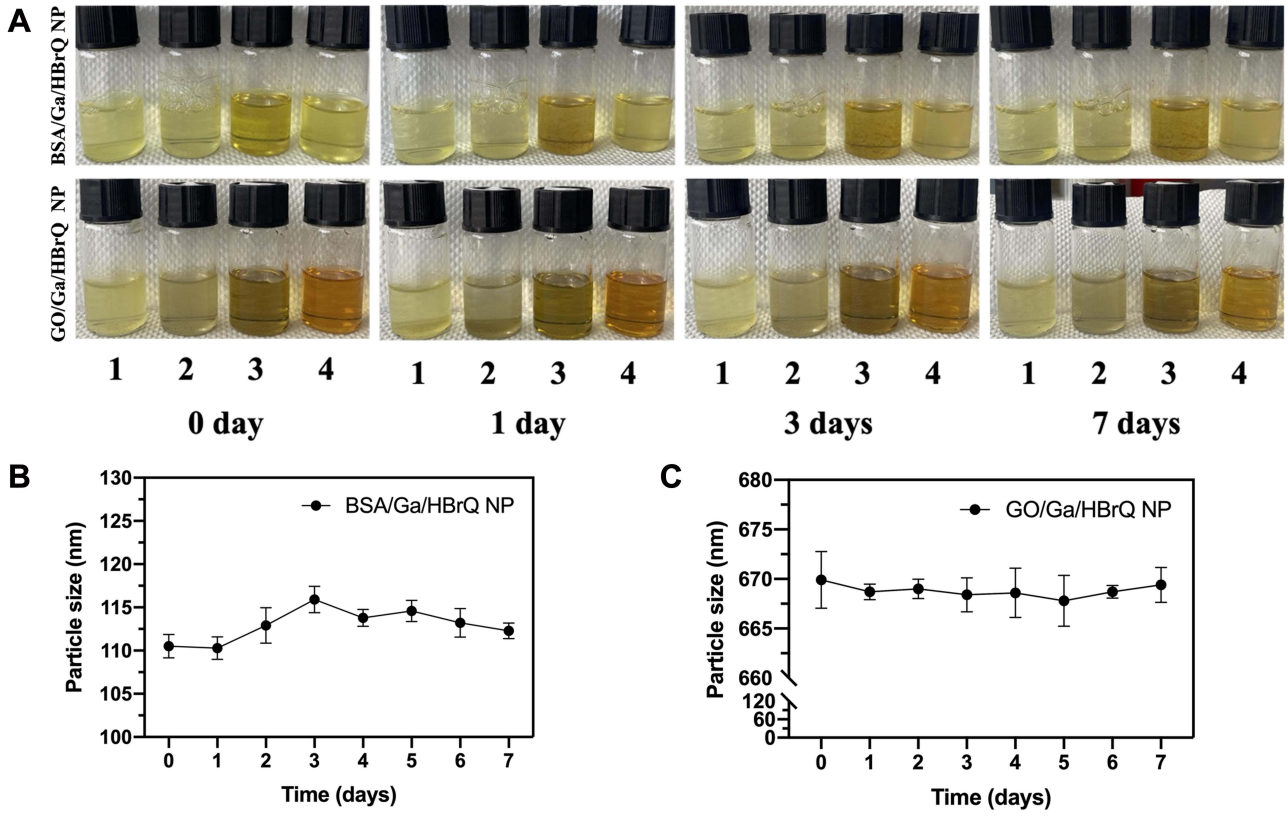

Figure 3 (**A**) Pictures of BSA/Ga/HBrQ NPs and GO/Ga/HBrQ NPs dissolved in different physiological solutions at different time points (1:H_2O 2:PBS 3:DMSO 4:DMF); (**B**) Variation of DLS average particle size of BSA/Ga/HBrQ NPs and (**C**) GO/Ga/HBrQ NPs in deionized water at different times.

determined the IC50 values of Ga(III) +HBrQ complex for HCT116 (Figure S8A). The results showed that Ga(III) +HBrQ complex (1.23 μM) exhibited superior IC_{50} values than cisplatin (5.70 μM) and oxaliplatin (8.34 μM) after cells were co-incubated with the compounds for 72 hours. The two NPs exhibited significant cytotoxicity, mainly due to the metal-coordinated drugs in the nanoparticles that could effectively act via endocytosis into cancer cells.[56] Encouraged by these results, we further explored the anti-tumor mechanisms of both NPs in HTC116 cells.

BSA/Ga/HBrQ NPs and GO/Ga/HBrQ NPs Induces Cell Cycle Arrest in HCT-116

The distribution of the cell cycle was examined to ascertain how BSA/Ga/HBrQ NPs and GO/Ga/HBrQ NPs exert their therapeutic impact. Both the BSA/Ga/HBrQ NPs and GO/Ga/HBrQ NPs experienced significant S phase arrests, as shown in Figure 4, which further inhibited DNA replication and caused cell death.[57] Evidently, the S phase of the BSA/

Table 1 IC_{50} (μM) Values of Nano-Drugs Toward Various Tumor Cells After 48 Hours

Tumor Cell	Cisplatin	BSA/Ga/HBrQ NPs	GO/Ga/HBrQ NPs
HCT116	9.08 ± 1.10	1.89 ± 0.14	4.75± 1.42
HeLa	4.94 ± 0.31	35.39 ± 4.02	30.57 ± 0.64
MDA-MB-231	12.21 ± 0.25	9.37 ± 0.94	1.57 ± 0.00
LO2	3.99 ± 0.74	5.85 ± 0.78	8.29 ± 0.04
SI[a]	0.44	3.09	1.74
SI[b]	0.81	0.16	0.27
SI[c]	0.33	0.62	5.28

Note: [a]SI=IC_{50}(LO2)/IC_{50}(HCT116), [b]SI=IC_{50}(LO2)/IC_{50}(HeLa), [c]SI=IC_{50}(LO2)/IC_{50}(MDA-MB-231).

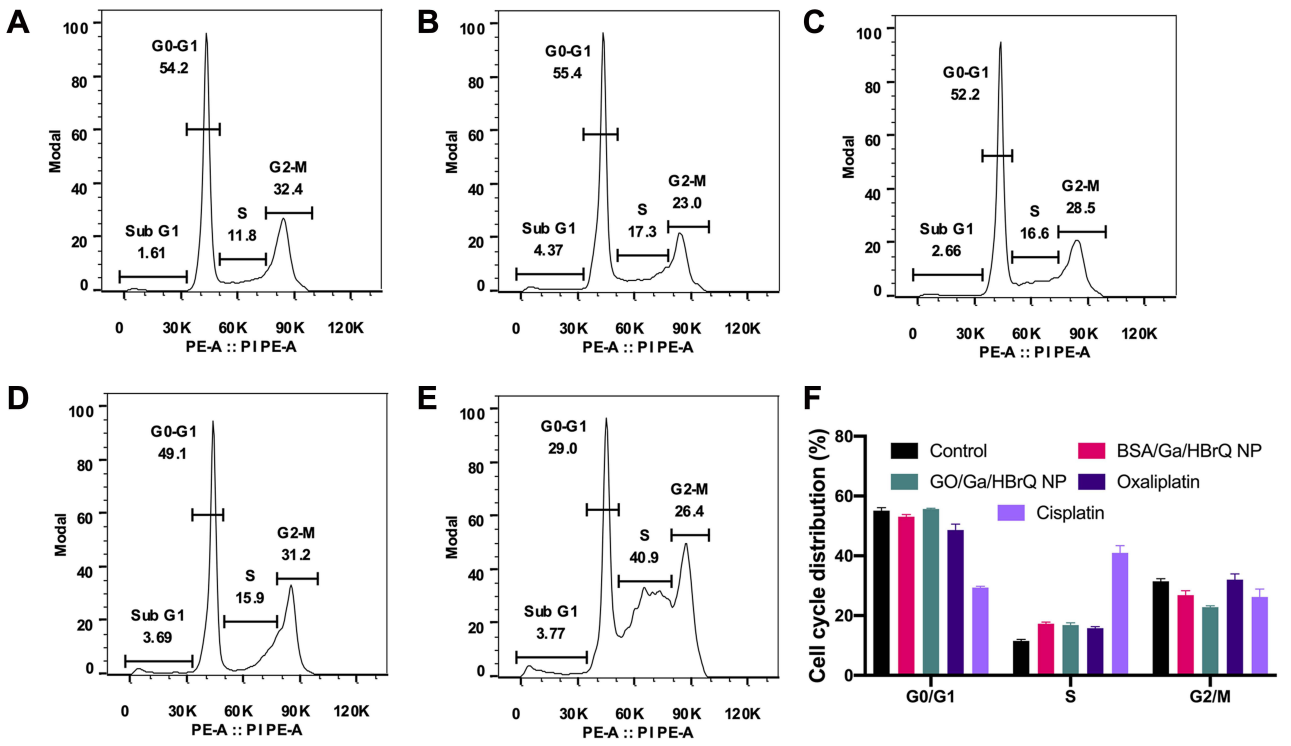

Figure 4 HCT116 cells were treated with 10 μM (**A**) control, (**B**) GO/Ga/HBrQ NPs, (**C**) BSA/Ga/HBrQ NPs, (**D**) Oxaliplatin (**E**) and Cisplatin, at the indicated concentrations, after which they were stained with PI and analyzed by flow cytometry. (**F**) Populations for cell cycle distribution.

Ga/HBrQ NPs and GO/Ga/HBrQ NPs were 15.06 and 21.86%, respectively, indicating that the GO/Ga/HBrQ NPs processed HCT116 cells more severely, as seen in the cell apoptosis assay. According to the findings, BSA/Ga/HBrQ NPs and GO/Ga/HBrQ NPs affect the S phase in HCT116 cells but have no effect on the G0/G1 or G2/M phases. This is consistent with the results of Ga(III) + HBrQ complex on HCT116 inhibition of cell cycle (Figure S8B).

BSA/Ga/HBrQ NPs and GO/Ga/HBrQ NPs Induces Apoptosis in HCT-116

Apoptosis is a key process in the development and progression of cancer.[58] Using labeling with Annexin V-FITC and propidium iodide (PI), apoptosis testing can be performed.[59] As shown in Figure 5, BSA/Ga/HBrQ NPs and GO/Ga/HBrQ NPs (10 μM) showed apoptosis-inducing characteristics, the apoptosis ratios were 14.8% and 23.2%, respectively. In contrast, the apoptosis ratio of BSA/Ga/HBrQ NPs and GO/Ga/HBrQ NPs at the same concentration were higher than that of oxaliplatin (13.5%), and the apoptosis ratio of GO/Ga/HBrQ NPs was higher than that of cisplatin (17.2%) (Figure 5F), indicating that the GO/Ga/HBrQ NPs showed higher toxicity than oxaliplatin and cisplatin. The higher apoptosis rate of HCT116 cells induced by BSA/Ga/HBrQ NPs and GO/Ga/HBrQ NPs may be due to the improved internalization of tumor cells to NPs with Ga(III) + HBrQ complex,[60] (Figure S18C). In addition, the data of apoptosis assay were consistent with the above MTT assay results.

BSA/Ga/HBrQ NPs and GO/Ga/HBrQ NPs Increases Reactive Oxygen Species (ROS) in HCT-116

Reactive oxygen species (ROS) are hypothesized to control apoptosis signal transduction mechanisms and play a significant part in the process of cell death[61,62] In this study, we employ 2',7'-dichlorodihydrofluorescein diacetate (DCFH-DA) as a fluorescent dye to detect ROS production in HCT116 cells. As shown in Figure 6A, the control group treated with PBS produced a small amount of ROS, probably due to naturally presented ROS.[60] However, as proof of desired ROS production, two NPs, cisplatin and oxaliplatin, demonstrated significant DCF green fluorescence. Among them, GO/Ga/HBrQ NPs were found to have a slightly higher fluorescence intensity. The outcomes of fluorescence

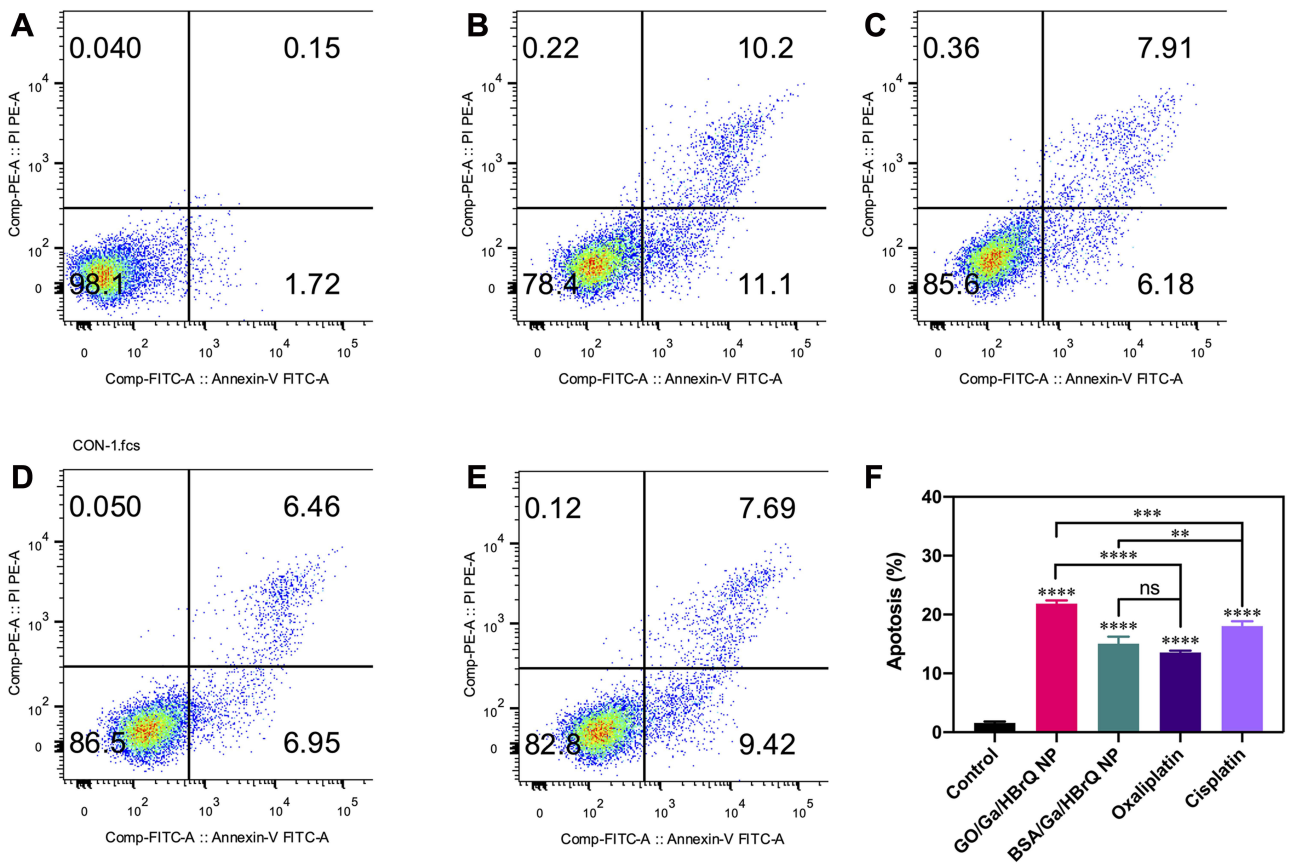

Figure 5 Effect of the apoptosis. Quantification of Annexin-V and PI double-stained HCT116 cells after treatment with 10 μM (**A**) control, (**B**) GO/Ga/HBrQ NPs, (**C**) BSA/Ga/HBrQ NPs, (**D**) Oxaliplatin (**E**) and Cisplatin at the indicated concentrations by flow cytometric; (**F**) Apoptosis ratio. **p < 0.01, ***p < 0.001, ****p < 0.0001, ns means no significant.

imaging were consistent with the quantitative fluorescence analysis measured by flow cytometry (Figure 6C and D). ROS production has been elevated in cancerous cells treated with BSA/Ga/HBrQ NPs and GO/Ga/HBrQ NPs,[63] which causes oxidative stress in the cells. The mitochondrial antioxidant protein mitoquinone counteracts this elevated ROS production, resulting in cell death.[64] This is consistent with the results of Ga(III)+HBrQ complex on the generation of intracellular ROS in HCT116 cells (Figure S8D).

BSA/Ga/HBrQ NPs and GO/Ga/HBrQ NPs Reduced Mitochondrial Transmembrane Potential

One of the main components of cell apoptosis is the decrease of mitochondrial membrane potential. The onset of early cell apoptosis is indicated by a reduction in mitochondrial membrane potential.[65] A popular fluorescent probe for measuring mitochondrial membrane potential is JC-1. JC-1 aggregates in the mitochondrial matrix to create a polymer that produces red fluorescence when the mitochondrial membrane potential is high. When the mitochondrial membrane potential is low, JC-1 exists as a monomer and exhibits green fluorescence. As a result, the JC-1 fluorescence color change makes detecting a decrease in mitochondrial membrane potential simple.[66] In our study, green fluorescence was observed in HCT116 cells incubated with BSA/Ga/HBrQ NPs and GO/Ga/HBrQ NPs, while red fluorescence was observed in the mitochondria of control cells (Figure 7). These findings imply that drug intervention reduces mitochondrial membrane potential, resulting in impaired mitochondrial function and, as a result, further induction of apoptosis. GO/Ga/HBrQ NPs have significantly higher green fluorescence intensity than the others. The findings suggest that apoptosis induced by BSA/Ga/HBrQ NPs and GO/Ga/HBrQ NPs may involve the intrinsic mitochondrial pathway.[67]

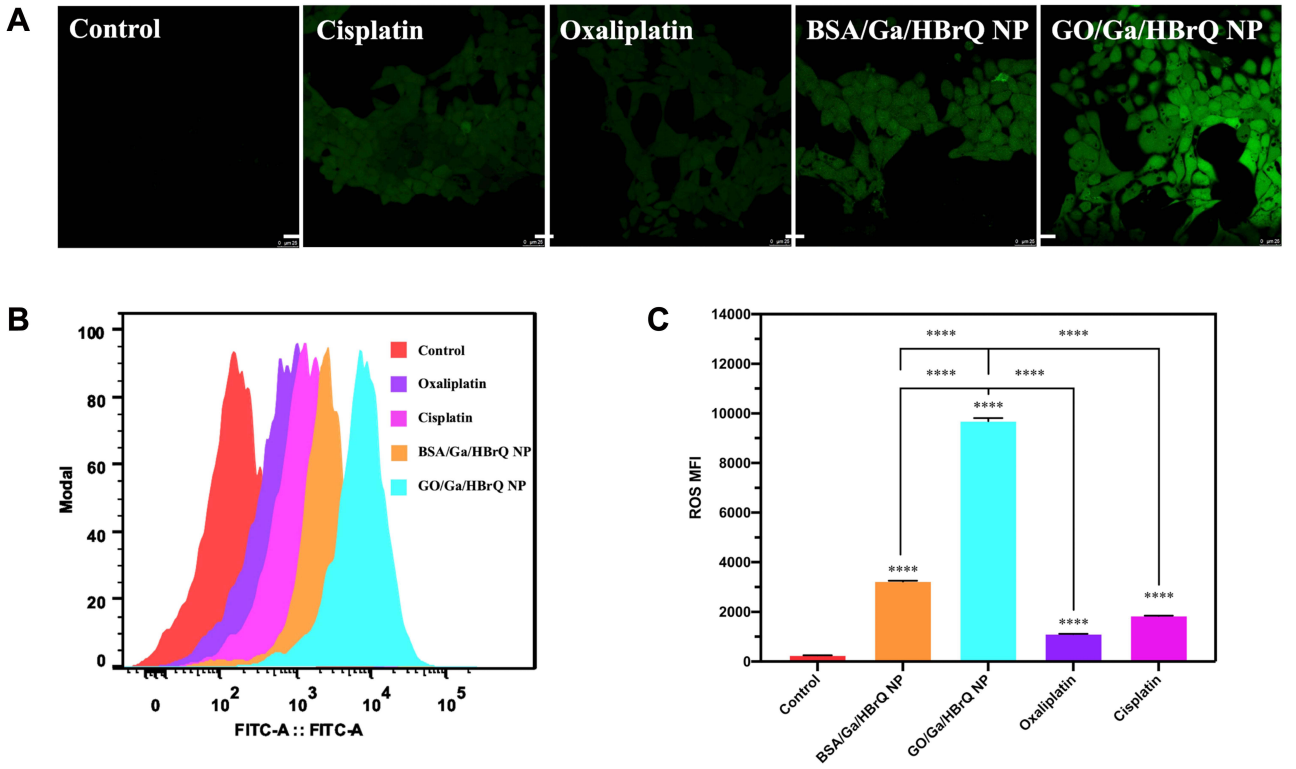

Figure 6 (**A**) Confocal laser scanning microscope images of Intracellular ROS detection in HCT116 cells incubated with PBS or NPs (10 μM) treatment, and (**B**) corresponding fluorescence intensity; (**C**) Original histograms for determination of ROS in HCT116 cells by the flow cytometry; The scale bar is 25 μm. ****p < 0.0001.

In vivo Tumor-Targeting Efficiency of BSA/Ga/HBrQ NPs and GO/Ga/HBrQ NPs

We evaluated the in vivo imaging ability and tumor targeting effect of BSA/Ga/HBrQ NPs and GO/Ga/HBrQ NPs due to their superior capacity to suppress tumor growth at the cellular level. To begin, in vivo imaging was performed in HCT116 tumor-bearing mice using a PerkinElmer IVIS imaging system to track the accumulation of BSA/Ga/HBrQ NPs and GO/Ga/HBrQ NPs (Figure 8A) at the tumor site. The fluorescence lifetimes of BSA/Ga/HBrQ NPs and GO/Ga/HBrQ NPs in air are 1.9382 ns and 1.6818 ns, respectively, which differ slightly from the 1.9634 ns of the Ga(III) + HBrQ complex (Figures S9 and S10).

As shown in Figure 8A, fluorescence signals appeared at the tumor site of mice 2 hours after intravenous injection of two nanomedicines. At 12 hours, the fluorescence signals of two nanomedicines were significantly enhanced at tumor sites, indicating the nanomedicines' good targeting ability. As shown in Figure 8B, the intensity of fluorescence in the tumor site was reduced 48 hours after injection compared to 24 hours, indicating that the nanoparticles were gradually metabolized out of the body. The mean fluorescence intensity of tumor sites treated with GO/Ga/HBrQ NPs mice was approximately 1.7 times higher than that of BSA/Ga/HBrQ NP treatment. The results show that BSA/Ga/HBrQ NPs and GO/Ga/HBrQ NPs, particularly GO/Ga/HBrQ NPs, have excellent ability of targeting tumor site.

Conclusion

The main problems with current metal-organic complex-based medicines are their limited water solubility and rapid circulation times. Therefore, increasing the biocompatibility of metal-organic combination medications is essential to increasing their efficacy. Here, we employing BSA and GO as a nanoreactor, two novel biocompatible nanomedicines-BSA/Ga/HBrQ NPs and GO/Ga/HBrQ NPs-were effectively created. The average sizes of BSA/Ga/HBrQ NPs and GO/Ga/HBrQ NPs were ca. 110 nm and 669 nm, respectively, and both of the two nanomedicines had drug loadings of 45.27% and 48.18% in PBS buffers. The BSA/Ga/HBrQ NPs (IC_{50} 1.89 μM) and GO/Ga/HBrQ NPs (IC_{50} 4.75 μM) displayed significantly higher cytotoxicity against HCT116 cells than did cisplatin (IC_{50} 9.08 μM) and oxaliplatin (IC_{50}

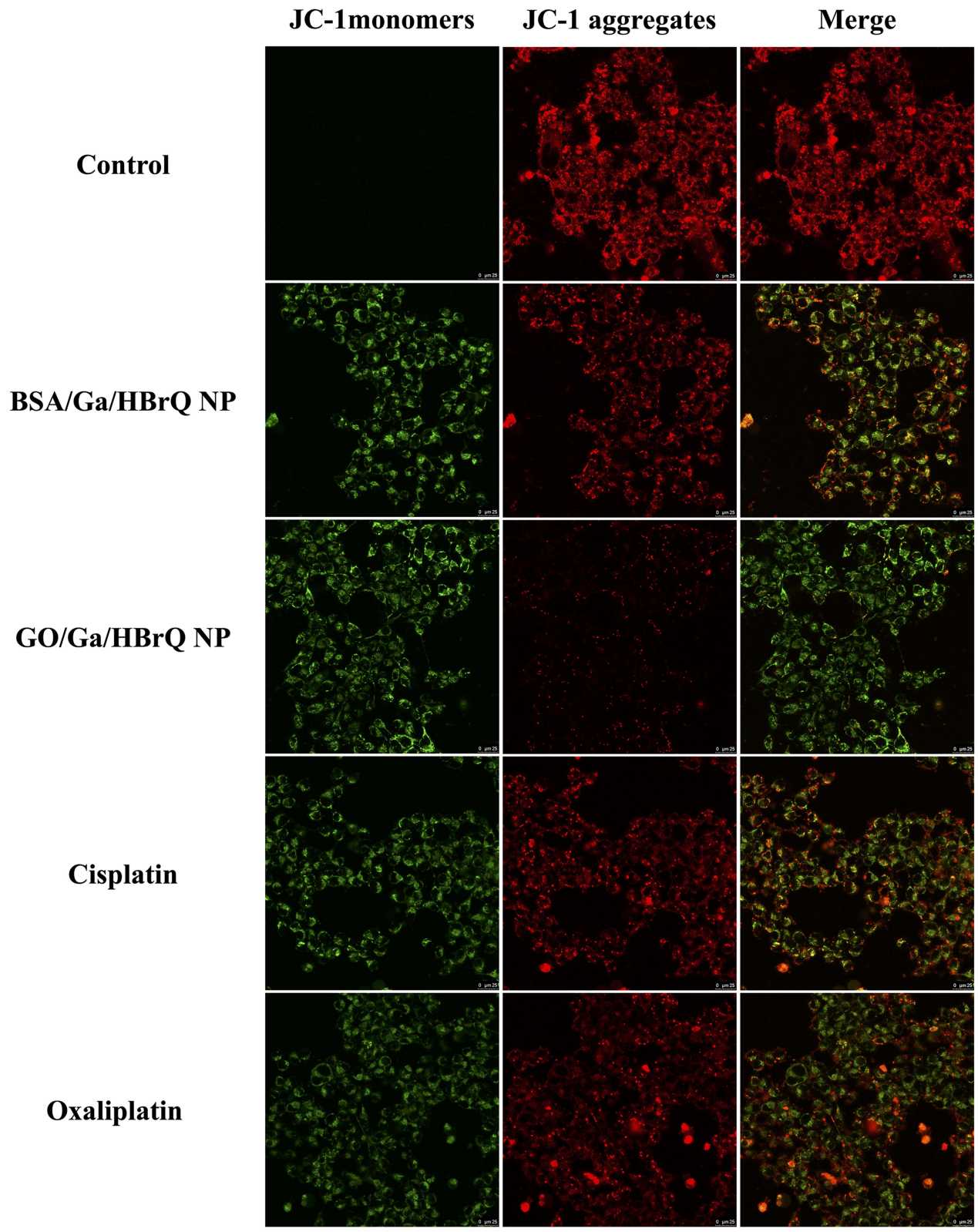

Figure 7 Mitochondrial membrane potential destruction of HCT116 cells induced with PBS or NPs by using JC-1 as fluorescence probe; The scale bar is 25 μm.

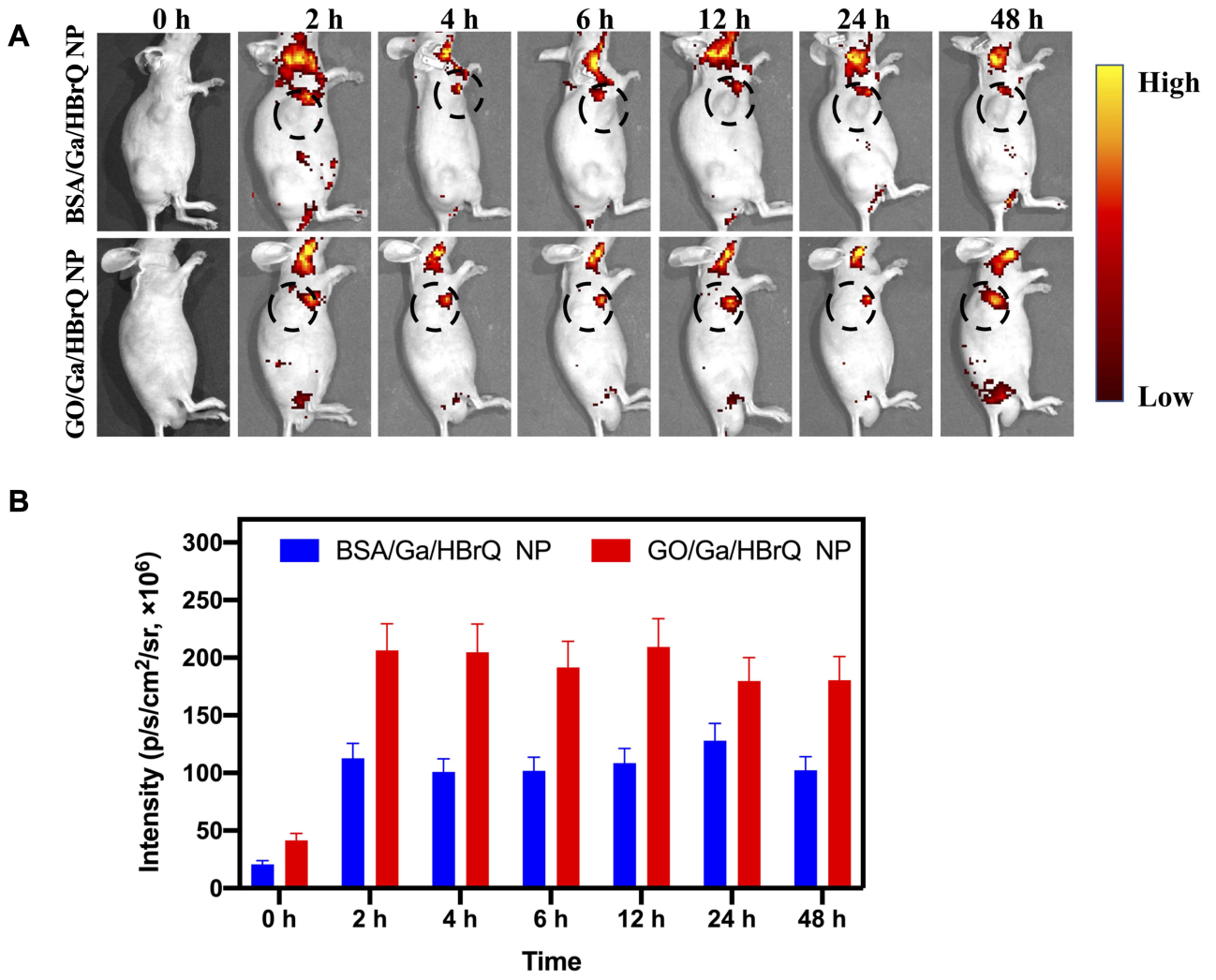

Figure 8 (**A**) In vivo fluorescence images of HCT116 tumor-bearing mice after intravenous injection of free BSA/Ga/HBrQ and GO/Ga/HBrQ nano-drugs at different time points (excitation: 420 nm; emission: 540 nm). (**B**) Quantitative calculation of fluorescence intensity at tumor sites over time.

8.34 μM), respectively, since these particles could be absorbed effectively. Additionally, the superior emissive properties of BSA/Ga/HBrQ NPs and GO/Ga/HBrQ NPs allow their use for in vivo imaging allowing highly effective therapy in HCT116 tumor-bearing mouse models. Owing to the excellent therapeutic efficacy, BSA/Ga/HBrQ NPs and GO/Ga/HBrQ NPs with a facile preparation method had great potential as anticancer agents for clinical application. This work suggests metal complex nanoparticles loaded with GO maybe better for drug delivery.

Acknowledgments

This work was financially supported by the National Natural Science Foundation of China (grant no. 21967019 and 21977080), and Yunnan Province Young and middle-aged academic and technical leaders Program 2011CI002. The authors thank the Advanced Analysis and Measurement Center of Yunnan University for the sample testing service. The authors would like to thank Tong Qi from Shiyanjia Lab (www.shiyanjia.com) for the mechanism of anticancer in vitro and imaging and biodistribution analysis in vivo.

Disclosure

There is no conflict to declare.

References

1. Chitambar CR. Gallium and its competing roles with iron in biological systems. *Biochim Biophys Acta*. 2016;1863(8):2044–2053. doi:10.1016/j.bbamcr.2016.04.027
2. Bernstein LR. Mechanisms of therapeutic activity for gallium. *Pharmacol Rev*. 1998;50(4):665–682.
3. Chitambar CR. Medical applications and toxicities of gallium compounds. *Int J Environ Res Public Health*. 2010;7(5):2337–2361. doi:10.3390/ijerph7052337
4. Frezza M, Verani CN, Chen D, Dou QP. The therapeutic potential of gallium-based complexes in anti-tumor drug design. *Lett Drug Des Discov*. 2007;4(5):311–317. doi:10.2174/157018007780867799
5. Newman RA, Brody AR, Krakoff IH. Gallium nitrate (NSC-15200) induced toxicity in the rat. A pharmacologic, histopathologic and micro-analytical investigation. *Cancer*. 1979;44(5):1728–1740. doi:10.1002/1097-0142(197911)44:5<1728::AID-CNCR2820440529>3.0.CO;2-S
6. Levina A, Crans DC, Lay PA. Speciation of metal drugs, supplements and toxins in media and bodily fluids controls in vitro activities. *Coord Chem Rev*. 2017;352:473–498. doi:10.1016/j.ccr.2017.01.002
7. Timerbaev AR. Advances in developing tris (8-quinolinolato) gallium (III) as an anticancer drug: critical appraisal and prospects. *Metallomics*. 2009;1(3):193–198. doi:10.1039/b902861g
8. Hofheinz R, Dittrich C, Jakupec M, et al. Early results from a Phase I study on orally administered tris (8-quinolinolato) gallium (III)(FFC11, KP46) in patients with solid tumors--a CESAR study (Central European Society for Anticancer Drug Research--EWIV). *Int J Clin Pharmacol Ther*. 2005;43(12):590–591. doi:10.5414/cpp43590
9. Kaluderović GN, Paschke R. Anticancer metallotherapeutics in preclinical development. *Curr Med Chem*. 2011;18(31):4738–4752. doi:10.2174/092986711797535308
10. Bernstein LR, Trevor T, Claire G, Bruce N. Chemistry and pharmacokinetics of gallium maltolate, a compound with high oral gallium bioavailability. *Met Based Drugs*. 2000;7(1):33–47. doi:10.1155/MBD.2000.33
11. Chitambar CR, Purpi DP, Woodliff J, Yang M, Wereley JP. Development of gallium compounds for treatment of lymphoma: gallium maltolate, a novel hydroxypyrone gallium compound, induces apoptosis and circumvents lymphoma cell resistance to gallium nitrate. *J Pharmacol Exp Ther*. 2007;322(3):1228–1236. doi:10.1124/jpet.107.126342
12. Galanski M, Arion VB, Jakupec MA, Keppler BK. Recent developments in the field of tumor-inhibiting metal complexes. *Curr Pharm Des*. 2003;9(25):2078–2089. doi:10.2174/1381612033454180
13. Peng -X-X, Gao S, Zhang J-L. Gallium (III) complexes in cancer chemotherapy. *Eur J Inorg Chem*. 2022;2022:e202100953. doi:10.1002/ejic.202100953
14. Chitambar CR. Gallium-containing anticancer compounds. *Future Med Chem*. 2012;4(10):1257–1272. doi:10.4155/fmc.12.69
15. Lessa JA, Parrilha GL, Beraldo H. Gallium complexes as new promising metallodrug candidates. *Inorganica Chim Acta*. 2012;393:53–63. doi:10.1016/j.ica.2012.06.003
16. Zhang H-R, Liu Y-C, Chen Z-F, et al. Studies on the structures, cytotoxicity and apoptosis mechanism of 8-hydroxylquinoline rhodium(iii) complexes in T-24 cells. *New J Chem*. 2016;40(7):6005–6014. doi:10.1039/C6NJ00182C
17. Zhang H-R, Huang K-B, Chen Z-F, et al. Cobalt(ii) 8-hydroxyquinoline complexes: structure, cytotoxicity and action mechanism. *MedChemComm*. 2016;7(5):806–812. doi:10.1039/C6MD00073H
18. Xian Chong S, Chik Fun Au-Yeung S, Kin Wah To K. Monofunctional platinum (PtII) Compounds–shifting the paradigm in designing new pt-based anticancer agents. *Curr Med Chem*. 2016;23(12):1268–1285. doi:10.2174/0929867323666160311114509
19. Dilruba S, Kalayda GV. Platinum-based drugs: past, present and future. *Cancer Chemother Pharmacol*. 2016;77(6):1103–1124. doi:10.1007/s00280-016-2976-z
20. Peng K, Liang -B-B, Liu W, Mao Z-W. What blocks more anticancer platinum complexes from experiment to clinic: major problems and potential strategies from drug design perspectives. *Coord Chem Rev*. 2021;449:214210. doi:10.1016/j.ccr.2021.214210
21. Niazvand F, Cheshmi A, Zand M, et al. An overview of the development of composites containing Mg and Zn for drug delivery. *J Compos Compd*. 2020;2(5):193–204. doi:10.29252/jcc.2.4.4
22. Asadi E, Chimeh AF, Hosseini S, et al. A review of clinical applications of graphene quantum dot-based composites. *J Compos Compd*. 2019;1(1):31–40. doi:10.29252/jcc.1.1.6
23. Zhou Z, Wang Y, Peng F, et al. Intercalation-activated layered MoO(3) nanobelts as biodegradable nanozymes for tumor-specific photo-enhanced catalytic therapy. *Angew Chem Int Ed Engl*. 2022;61(16):e202115939. doi:10.1002/anie.202115939
24. Kheradmand Z, Rabiei M, Tahneh AN, et al. Targeted drug delivery by bone cements. *J Compos Compd*. 2022;4(10):59–73. doi:10.52547/jcc.4.1.7
25. Nasr Azadani R, Sabbagh M, Salehi H, Cheshmi A, Beena Kumari A, Erabi G. Sol-gel: uncomplicated, routine and affordable synthesis procedure for utilization of composites in drug delivery: review. *J Compos Compd*. 2021;2:57–70. doi:10.52547/jcc.3.1.6
26. Tan X, Liao D, Rao C, et al. Recent advances in nano-architectonics of metal-organic frameworks for chemodynamic therapy. *J Solid State Chem*. 2022:123352. doi:10.1016/j.jssc.2022.123352
27. Hu T, Gu Z, Williams GR, et al. Layered double hydroxide-based nanomaterials for biomedical applications. *Chem Soc Rev*. 2022;51(14):6126–6176. doi:10.1039/d2cs00236a
28. Ding Q, Xu Z, Zhou L, et al. A multimodal metal-organic framework based on unsaturated metal site for enhancing antitumor cytotoxicity through chemo-photodynamic therapy. *J Colloid Interface Sci*. 2022;621:180–194. doi:10.1016/j.jcis.2022.04.078
29. Zhao X, He X, Hou A, et al. Growth of Cu2O nanoparticles on two-dimensional Zr–ferrocene–metal–organic framework nanosheets for photothermally enhanced chemodynamic antibacterial therapy. *Inorg Chem*. 2022;61(24):9328–9338. doi:10.1021/acs.inorgchem.2c01091
30. Li M, Yin S, Lin M, et al. Current status and prospects of metal–organic frameworks for bone therapy and bone repair. *J Mater Chem B*. 2022;10(27):5105–5128. doi:10.1039/D2TB00742H
31. Li Z, Xiao C, Yong T, Li Z, Gan L, Yang X. Influence of nanomedicine mechanical properties on tumor targeting delivery. *Chem Soc Rev*. 2020;49(8):2273–2290. doi:10.1039/C9CS00575G
32. Johnstone TC, Suntharalingam K, Lippard SJ. The next generation of platinum drugs: targeted Pt(ii) agents, nanoparticle delivery, and Pt(IV) prodrugs. *Chem Rev*. 2016;116(5):3436–3486. doi:10.1021/acs.chemrev.5b00597

33. Mignani S, Bryszewska M, Klajnert-Maculewicz B, Zablocka M, Majoral J-P. Advances in combination therapies based on nanoparticles for efficacious cancer treatment: an analytical report. *Biomacromolecules*. 2015;16(1):1–27. doi:10.1021/bm501285t
34. Sun W, Li S, Haupler B, et al. An amphiphilic ruthenium polymetallodrug for combined photodynamic therapy and photochemotherapy in vivo. *Adv Mater*. 2017;29:1603702. doi:10.1002/adma.201603702
35. Niazvand F, Wagh PR, Khazraei E, Dastjerdi MB, Patil C, Najar IA. Application of carbon allotropes composites for targeted cancer therapy drugs: a review. *J Compos Compd*. 2021;3(7):140–151. doi:10.52547/jcc.3.2.7
36. Abd Al-jabbar S, Atiroğlu V, Hameed RM, et al. Fabrication of dopamine conjugated with protein @metal organic framework for targeted drug delivery: a biocompatible pH-Responsive nanocarrier for gemcitabine release on MCF-7 human breast cancer cells. *Bioorg Chem*. 2022;118:105467. doi:10.1016/j.bioorg.2021.105467
37. Duan Q, Shi J, Zhou L, Zhang B, Wang X, Sang S. pH-responsive and sustained release drug delivery system of BSA coated CDs-DOX. *J Mol Struct*. 2022;1248:131358. doi:10.1016/j.molstruc.2021.131358
38. Kaboli SF, Mehrnejad F, Nematollahzadeh A. Molecular modeling prediction of albumin-based nanoparticles and experimental preparation, characterization, and in-vitro release kinetics of prednisolone from the nanoparticles. *J Drug Deliv Sci Technol*. 2021;64:102588. doi:10.1016/j.jddst.2021.102588
39. Krasteva N, Staneva D, Vasileva B, Miloshev G, Georgieva M. Bioactivity of PEGylated graphene oxide nanoparticles combined with near-infrared laser irradiation studied in colorectal carcinoma cells. *Nanomaterials*. 2021;11(11):3061. doi:10.3390/nano11113061
40. Chen H, Xing L, Guo H, Luo C, Zhang X. Dual-targeting SERS-encoded graphene oxide nanocarrier for intracellular co-delivery of doxorubicin and 9-aminoacridine with enhanced combination therapy. *Analyst*. 2021;146(22):6893–6901. doi:10.1039/D1AN01237A
41. Hu D, Xu H, Xiao B, et al. Albumin-stabilized metal–organic nanoparticles for effective delivery of metal complex anticancer drugs. *ACS Appl Mater Interfaces*. 2018;10(41):34974–34982. doi:10.1021/acsami.8b12812
42. El-Sonbaty SM, Moawed FS, Kandil EI, Antitumor AMT. Antibacterial efficacy of gallium nanoparticles coated by ellagic acid. *Dose Response*. 2022;20(1):15593258211068998. doi:10.1177/15593258211068998
43. Mohan Viswanathan T, Krishnakumar V, Senthilkumar D, et al. Combinatorial delivery of gallium (III) nitrate and curcumin complex-loaded hollow mesoporous silica nanoparticles for breast cancer treatment. *Nanomaterials*. 2022;12(9):1472. doi:10.3390/nano12091472
44. Yang T, Wang Y, Ke H, et al. Protein-nanoreactor-assisted synthesis of semiconductor nanocrystals for efficient cancer theranostics. *Adv Mater*. 2016;28(28):5923–5930. doi:10.1002/adma.201506119
45. Zhao R, Lv M, Li Y, et al. Stable nanocomposite based on PEGylated and silver nanoparticles loaded graphene oxide for long-term antibacterial activity. *ACS Appl Mater Interfaces*. 2017;9(18):15328–15341. doi:10.1021/acsami.7b03987
46. Williams HD, Trevaskis NL, Charman SA, et al. Strategies to address low drug solubility in discovery and development. *Pharmacol Rev*. 2013;65(1):315–499. doi:10.1124/pr.112.005660
47. Zhang C, Wang W, Liu T, et al. Doxorubicin-loaded glycyrrhetinic acid-modified alginate nanoparticles for liver tumor chemotherapy. *Biomaterials*. 2012;33(7):2187–2196. doi:10.1016/j.biomaterials.2011.11.045
48. Vogler A, Kunkely H. Photochemistry of peroxo complexes induced by LMCT, MLCT and peroxide IL/LLCT excitation. *Coord Chem Rev*. 2006;250(13–14):1622–1626. doi:10.1016/j.ccr.2005.10.009
49. Jaworska M, Malecki JG. A density functional study of the electronic and geometrical structures of RuCl2(PPh3)(2)(HPz)(2) isomers and electronic spectrum of cis, cis, cis complex. *J Mol Struct*. 2006;784(1–3):169–176. doi:10.1016/j.molstruc.2005.09.017
50. Ren G-Q, Pei G-X, Zhang J-C, Li W-Z. Activity promotion of anti-sintering AuGMgGa(2)O(4) using ceria in the water gas shift reaction and catalytic combustion reactions. *Chin J Catal*. 2019;40(4):600–608. doi:10.1016/s1872-2067(19)63295-x
51. Xie Q, Miao C, Hua W, Yue Y, Gao Z. Ga-doped MgAl2O4 spinel as an efficient catalyst for ethane dehydrogenation to ethylene assisted by CO2. *Ind Eng Chem Res*. 2021;60(31):11707–11714. doi:10.1021/acs.iecr.1c01641
52. Du J-Z, Du X-J, Mao C-Q, Wang J. Tailor-made dual pH-sensitive polymer–doxorubicin nanoparticles for efficient anticancer drug delivery. *J Am Chem Soc*. 2011;133(44):17560–17563. doi:10.1021/ja207150n
53. Rondeau P, Armenta S, Caillens H, Chesne S, Bourdon E. Assessment of temperature effects on β-aggregation of native and glycated albumin by FTIR spectroscopy and PAGE: relations between structural changes and antioxidant properties. *Arch Biochem Biophys*. 2007;460(1):141–150. doi:10.1016/j.abb.2007.01.014
54. Gallier J, Rivet P, de Certaines J. 1H- and 2H-NMR study of bovine serum albumin solutions. *Biochim Biophys Acta*. 1987;915(1):1–18. doi:10.1016/0167-4838(87)90119-1
55. Hong BJ, Compton OC, An Z, Eryazici I, Nguyen ST. Successful stabilization of graphene oxide in electrolyte solutions: enhancement of biofunctionalization and cellular uptake. *ACS Nano*. 2012;6(1):63–73. doi:10.1021/nn202355p
56. Zhang S, Gao H, Bao G. Physical principles of nanoparticle cellular endocytosis. *ACS Nano*. 2015;9(9):8655–8671. doi:10.1021/acsnano.5b03184
57. Zhao F, Wang H, Kunda P, Chen X, Liu QL, Liu T. Artesunate exerts specific cytotoxicity in retinoblastoma cells via CD71. *Oncol Rep*. 2013;30(3):1473–1482. doi:10.3892/or.2013.2574
58. Saraste A, Pulkki K. Morphologic and biochemical hallmarks of apoptosis. *Cardiovasc Res*. 2000;45(3):528–537. doi:10.1016/s0008-6363(99)00384-3
59. Liu L-G, Sun Y-M, Liu Z-Y, et al. Halogenated gallium corroles: DNAinteraction and photodynamic antitumor activity. *Inorg Chem*. 2021;60(4):2234–2245. doi:10.1021/acs.inorgchem.0c03016
60. Ji P, Huang H, Yuan S, et al. ROS-mediated apoptosis and anticancer effect achieved by artesunate and auxiliary Fe(II) released from ferriferous oxide-containing recombinant apoferritin. *Adv Health Care Mater*. 2019;8(23):e1900911. doi:10.1002/adhm.201900911
61. Wang Y, He Q-Y, Sun RW-Y, Che C-M, Chiu J-F. Gold(III) porphyrin 1a induced apoptosis by mitochondrial death pathways related to reactive oxygen species. *Cancer Res*. 2005;65(24):11553–11564. doi:10.1158/0008-5472.Can-05-2867
62. Gorrini C, Harris IS, Mak TW. Modulation of oxidative stress as an anticancer strategy. *Nat Rev Drug Discov*. 2013;12(12):931–947. doi:10.1038/nrd4002
63. Harini L, Karthikeyan B, Srivastava S, et al. Polyethylenimine-modified curcumin-loaded mesoporus silica nanoparticle (MCM-41) induces cell death in MCF-7 cell line. *IET Nanobiotechnol*. 2017;11(1):57–61. doi:10.1049/iet-nbt.2016.0075
64. Kopparapu PK, Boorjian SA, Robinson BD, et al. Expression of VEGF and its receptors VEGFR1/VEGFR2 is associated with invasiveness of bladder cancer. *Anticancer Res*. 2013;33(6):2381–2390. doi:10.1002/jcb.21707

65. Green DR, Reed JC. Mitochondria and apoptosis. *Science*. 1998;281(5381):1309–1312. doi:10.1126/science.281.5381.1309
66. Takahashi A, Masuda A, Sun M, Centonze VE, Herman B. Oxidative stress-induced apoptosis is associated with alterations in mitochondrial caspase activity and Bcl-2-dependent alterations in mitochondrial pH (pHm). *Brain Res Bull*. 2004;62(6):497–504. doi:10.1016/j.brainresbull.2003.07.009
67. Qi J, Qian K, Tian L, Cheng Z, Wang Y. Gallium(iii)–2-benzoylpyridine-thiosemicarbazone complexes promote apoptosis through Ca2+ signaling and ROS-mediated mitochondrial pathways. *New J Chem*. 2018;42(12):10226–10233. doi:10.1039/C8NJ00697K